Energy Efficiency of Plasma Jets: Electrical Modeling Based on Experimental Results

Achraf Hani, Karim Saber, Alyen Abahazem, Nofel Merbahi

plasma

MDPI

Article

Energy Efficiency of Plasma Jets: Electrical Modeling Based on Experimental Results

Achraf Hani [1,*], Karim Saber [1], Alyen Abahazem [1,2] and Nofel Merbahi [3]

[1] Materials and Renewable Energies Laboratory, Ibn Zohr University, Agadir 80000, Morocco; mirak.rebas@gmail.com (K.S.); a.abahazem@uiz.ac.ma (A.A.)
[2] Laboratory of Sciences and Science Didactics (LASDIS), Regional Center for Education and Training Professions, Inezgane 80000, Morocco
[3] Plasma and Energy Conversion Laboratory (LAPLACE), Paul Sabatier University, 31062 Toulouse, France; merbahi@laplace.univ-tlse.fr
* Correspondence: achraf.hani@edu.uiz.ac.ma

Abstract: This paper focuses on the determination of and improvement in the energy efficiency of plasma jets. To achieve this goal, an equivalent electrical model of a discharge reactor was developed, incorporating variable electrical parameters. The evolution of these parameters was determined by a mathematical identification method based on the recursive least squares algorithm (RLSA). The good agreement between the measured currents and those calculated using our electrical circuit, as well as the significant shapes of the estimated parameters, confirmed the accuracy of the parameter estimation method. This allowed us to use these parameters to determine the energy delivered to the reactor and that used during the discharge. This made our reactor controllable at the energy level. Thus, the ratio between these two energies allowed us to calculate the energy efficiency of plasma jets at each discharge instant. We also studied the effect of the applied voltage on efficiency. We found that efficiency was increased from 75% to 90% by increasing the voltage from 6 kV to 8 kV. All the results found in this work were interpreted and compared with the discharge behavior. This proposed model will help us to choose the right operating conditions to reach the maximum efficiency.

Keywords: corona discharge; voltage measurement; current measurement; electrical model; discharge power; delivered power; plasma energy efficiency

Citation: Hani, A.; Saber, K.; Abahazem, A.; Merbahi, N. Energy Efficiency of Plasma Jets: Electrical Modeling Based on Experimental Results. *Plasma* **2024**, *7*, 826–841. https://doi.org/10.3390/plasma7040044

Academic Editors: Tariq Rafiq and Andrey Starikovskiy

Received: 25 July 2024
Revised: 19 October 2024
Accepted: 21 October 2024
Published: 23 October 2024

1. Introduction

In recent years, non-equilibrium atmospheric pressure plasma jets have been of great interest because of their many advantages. On the one hand, they have the advantage of micro-plasma stability at atmospheric pressure, and on the other hand, cold plasma jets are always created on the same principle: a channel of helium (or another easily ionized gas such as argon) is created in the ambient air by blowing helium through a tube, called an injector, which opens into the ambient air. There are several geometric configurations that create an electric field in the reactor. This field generates a plasma that will propagate outside and that is guided by the helium channel, which is more easily ionized than air. Moreover, by interacting with the ambient air, the jets create many reactive species, creating a chemically rich environment in and around the jet. There are many applications of plasmas, such as decontamination and biomedical applications [1–5], surface treatment to clean or deposit thin films [6–8], biomedicine [9–11], and nanomaterial synthesis [12,13].

In 1991, the first plasma jet at atmospheric pressure was developed by Koinuma et al. [14]. It was composed of a quartz tube with an internal electrode powered by radio frequency (RF) and an external electrode connected to the ground. Thus, the discharge gas was a mixture consisting primarily of helium. The addition of small quantities of gas, such as carbon tetrafluoride, CF_4, was intended to etch the silicon compounds and to aid in the study of its effect on the plasma. During the 2000s, the attention given to

plasma jets increased with the development of new configurations and a diversification of their application fields. In 2002, Stoffels et al. [15] presented a new system to generate a non-thermal micro-plasma at atmospheric pressure. They demonstrated that this plasma, initiated by RF excitation, is well suited for biomedical applications. In 2005, the team of M. Laroussi were the first to provide sufficient qualitative and quantitative data to establish the foundations of the understanding of the phenomena governing plasma jets. Lu and Laroussi [16] and Förster et al. [17] developed new systems capable of initiating, respectively, a helium and argon plasma microjet by applying a high-voltage pulsed power supply with a repetition rate from 1 kHz up to 25 kHz, which is ignited in a capillary dielectric barrier discharge, thus creating a jet that is several centimeters long. Subsequently, many works have developed these plasma microjets, each using a particular geometry; these include Teschke et al. [18], Zhang et al. [19], Walsh et al. [20], Cheng et al. [21], Kim et al. [22], and Hong et al. [23].

In this work, the focus is on helium plasma jets. This choice of gas and excitation source has been extensively studied and ensures both reproducible and stable discharge generation, as well as negligible gas heating, which is essential for biomedical applications. In general, for all plasma jets, the plasma emerges from the tube where it is generated, forming a visible jet that extends a few centimeters. Although the plasma jet appears continuous to the naked eye, it was first demonstrated by Teschke et al. (2005) [18], Lu and Laroussi (2006) [24], and Sands et al. (2008) [25] that it is actually created by ionization waves propagating at high speeds, ranging from 10 to 100 km/s, covering several centimeters in just a few hundred nanoseconds or microseconds. The discharge also propagates as an ionization wave. Therefore, many features of discharge dynamics are shared across different jet sources and frequencies.

In the early experimental [18,24,25] and numerical [26–30] studies on plasma jets, it was observed that the ionization waves in the jets are very similar to streamers, although they are guided by the buffer gas channel and are generally referred to as guided streamers. These ionization waves are transient but much more reproducible than classical streamers in air and do not involve the complexity of branching. Therefore, the study of plasma jets represents a unique opportunity, from a fundamental perspective, to better understand the physics of streamers, from their initiation to their interaction with surfaces.

In recent years, a number of equivalent electrical models have been developed and used to describe discharge characteristics and system behavior. These include approaches such as the use of a time-varying resistor, the application of a full diode bridge, or the use of a Self-Commutated Converter (SCC) in combination with a time-varying resistor [31–33]. Alternatively, some researchers have opted to model the DBD using an electrical circuit comprising a capacitor to represent the capacitive behavior of the dielectric barrier (C_d) and a capacitor for the gas (C_g). In this model, the gas is considered non-conductive as long as its voltage remains below a certain threshold value ($|v_{gas}| < Vth$). When breakdown occurs, the gas is then represented by a constant voltage ($v_{gas} = \pm Vth$). The parameters of this model, C_d, C_g, and Vth, are determined by analyzing experimental waveforms for the voltage and current flowing through the DBD [34–37].

As part of this research, we have introduced two significant improvements to this classical model. The first is the addition of a variable resistor to represent the current flow across the inter-electrode gap, replacing the fixed voltage which varies between $\pm$Vth. This resistor is connected in series with a variable capacitor to describe the behavior inside the tube. The second modification consists in incorporating an additional circuit to represent wave propagation outside the discharge tube. One of the main strengths of our approach lies in the use of time-varying electrical parameters to describe the discharge behavior at each instant. However, this has resulted in a more complex mathematical model, for which we use a method of parameter identification and experimental measurements. This method enables us to estimate the values of the electrical parameters of the proposed circuit, paving the way for further analysis of the dielectric barrier discharge. An essential element of this research is the validation of our improved electrical model. This is achieved by comparing

the experimentally measured current with that calculated by our circuit. The estimated parameters will be used to ensure the energy balance of the plasma and, more particularly, for the determination of its energy efficiency. Thus, this study allows us to control the discharge and to improve the efficiency by changing the operating conditions.

2. Experimental Apparatus

The atmospheric pressure plasma jet (APPJ) used in this study uses a dielectric barrier discharge (DBD) to generate a plasma. The schematic of the DBD plasma jet is presented in Figure 1. It consists of a quartz tube representing a dielectric barrier discharge. The length of the tube is about 95 mm, with a wall thickness of 2 mm, while the inner and outer diameters of the tube are 4 mm and 6 mm, respectively. The DBD plasma jet device is based on a double-ring structure with two aluminum ring electrodes covering the outer quartz tube. The width of the aluminum ring is 20 mm, the distance between two electrodes is 10 mm, and the distance between the downstream electrode and the quartz tube nozzle is 5 mm. This information is given in Figure 1a.

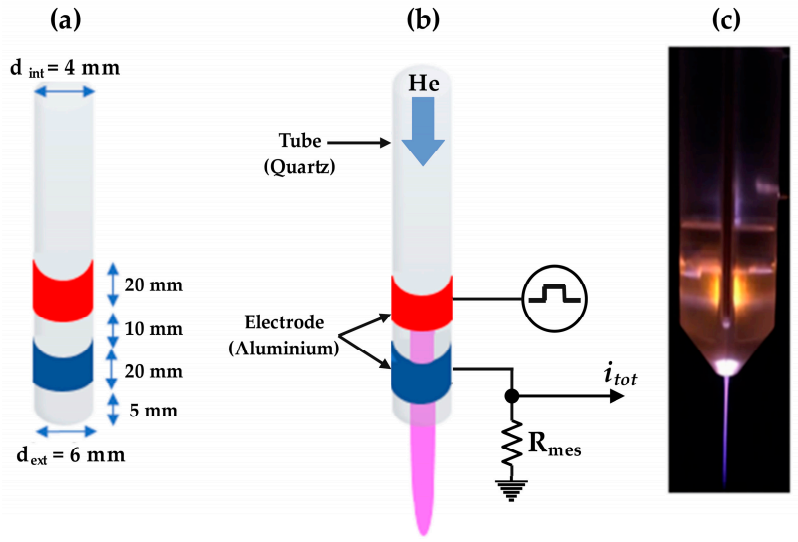

Figure 1. (**a**) Schematic of the DBD plasma source. (**b**) Helium jet device. (**c**) Photo of the plasma jet.

The assembly (quartz tube + electrodes) forms a DBD-type device, which allows us to avoid an arc passage. The device is supplied with helium 4.5 in the upper part of the tube, and the flow rate is controlled by a mass flow meter (Brooks instrument SLA 5800 Series) calibrated for helium. This device has the advantage of being insensitive to variations in gas pressure and temperature. The flow meter is controlled by the Brooks instrument 0254 control unit, allowing the gas flow rate to vary from 0 to 15 L/min. In this work, the helium flow rate is set to 3 L/min. Figure 1a,b shows the schematic of the device, and Figure 1c is a photograph of the helium plasma jet in operation.

In Figure 1b, the total current i_{tot} is measured across the resistor R_{mes} connected to the ground. This configuration captures both the discharge and capacitive currents generated within the plasma discharge. The voltage drop across R_{mes} is then used to calculate the total current flowing through the system.

For plasma jet excitation, we used a high-voltage pulse source, whose voltage can be adjusted in the range of 0–10 kV. The rise and fall time ranges from eighty nanoseconds to several hundred of nanoseconds, the frequency is adjustable in the range of 1 Hz to 10 kHz, the duty cycle can vary from 1% to 50%, and the pulse width from 250 ns to 1.75 s. The power supply is based on the principle of a series chopper. High-voltage DC is delivered by a Technix SR10-R-300 generator connected to a DEIPVX 4110 series high-voltage chopper, manufactured by Berkeley Nucleonics Corporation, San Rafael, CA, USA, and controlled by a low-frequency generator.

3. Electrical Model

Under the effect of the applied voltage, ionization inside the tube increases, leading to the generation of a streamer that propagates towards the ambient air through the tube's outlet. The length of this streamer progressively grows, allowing for the observation of the discharge evolution in the plasma jet reactor through three distinct modes: it begins with a corona discharge, then transitions to a dielectric barrier discharge, and finally results in the formation of a plasma jet, as indicated in reference [38]. In our study, the plasma jet reactor consists of a quartz tube, as illustrated in Figure 1, and includes two ring-shaped electrodes. Although the discharge principle is similar to that in reference [38], the symmetry of the electrodes limits the discharge evolution to two modes: dielectric barrier discharge followed by the plasma jet.

At each level of applied voltage, an equivalent electrical model of the discharge can be established to provide a complete representation of the plasma jet. When the applied voltage exceeds the breakdown voltage, the front of the electrical channel propagates from the high-voltage electrode to the grounded electrode, leaving behind charged particles (electrons, positive ions, negative ions, excited and metastable atoms). The characteristics of this discharge are similar to those of dielectric barrier discharges due to the symmetry of the two electrodes and the presence of a dielectric. This promotes the accumulation of charges on both the internal surface of the quartz tube and within it. Based on the quantity of charges generated during this discharge, we were able to propose an electrical model for the dielectric barrier discharge.

$$q_{tube} = q_{diel} + q_{dis} \tag{1}$$

Equation (1) expresses the amount of charge in the tube (q_{tube}), which corresponds to the sum of the charges accumulated on the dielectric surface (q_{diel}) and those generated in the tube's medium during streamer propagation. The charge quantity is then replaced by its integral during the discharge in order to obtain the current inside the tube (i_{tube}), as indicated in Equation (2), where i_{dis} and i_{diel} correspond to the current flowing in the medium and the dielectric current, respectively.

$$i_{tube} = i_{diel} + i_{dist} \tag{2}$$

This latter expression of the DBD illustrates an application of Kirchhoff's first law, allowing for the proposal of an electrical circuit with two branches. The first branch represents an equivalent dielectric circuit, acting as a capacitor, while the second branch corresponds to the equivalent electrical circuit of the streamer propagation from the high-voltage electrode to the grounded electrode. This streamer propagation phenomenon is modeled by a variable resistance, representing the formation of the streamer (electrical channel), in series with a variable capacitance, which reflects the space between the streamer head (first plate) and the grounded electrode (second plate) [39]. Thus, an equivalent electrical circuit for the discharge at this voltage level is obtained, as illustrated in Figure 2.

At a certain level of applied voltage, the electric field inside the tube becomes more intense, strengthening the electrical channel as it moves toward the ambient air, thereby producing a plasma jet. During this process, a charge is generated outside the reactor, in addition to that created inside the tube (DBD).

$$q_{tot} = q_{tube} + q_{jet} \tag{3}$$

Equation (3) expresses the total amount of charge q_{tot}, which corresponds to the sum of the charge created inside the quartz tube q_{tube} (Equation (1)) and the charge generated outside the reactor q_{jet}. The charge quantity was then replaced by its integral during the discharge, which allowed for the plasma jet discharge current i_{tot} to be obtained, as

indicated in Equation (4). In this equation, i_{tube} and i_{jet} represent the currents flowing through the tube (DBD) and the jet, respectively.

$$i_{tot} = i_{tube} + i_{jet} \tag{4}$$

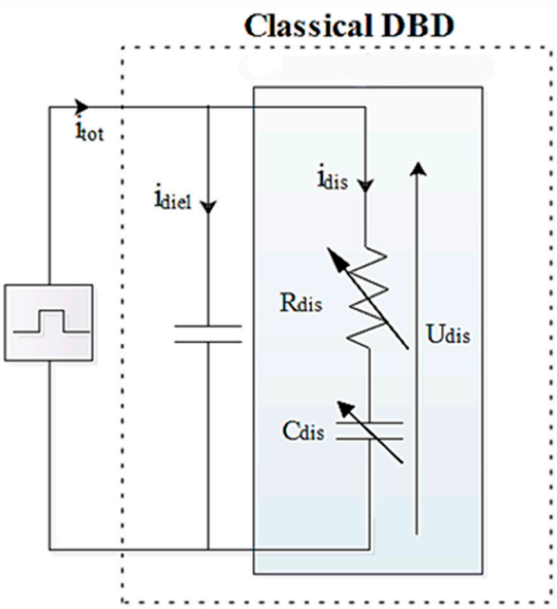

Figure 2. Electrical circuit equivalent to the dielectric barrier discharge (DBD).

This leads us to conclude that the plasma jet discharge current i_{tot} is the sum of the currents flowing through the tube i_{tube} and through the jet i_{jet}, in accordance with Kirchhoff's first law. We can thus propose an electrical circuit consisting of two parallel branches: the first represents the equivalent electrical model of the discharge inside the tube, similar to that of the dielectric barrier discharge (DBD) (Figure 2), while the second branch corresponds to the equivalent circuit of the plasma jet. Since the plasma jet forms a few centimeters from the tube's outlet through the ionization phenomenon, its behavior is akin to that of streamer propagation, which allows it to be modeled by a variable resistance in series with a variable capacitance. Finally, the equivalent circuit for the plasma jet discharge is illustrated in Figure 3.

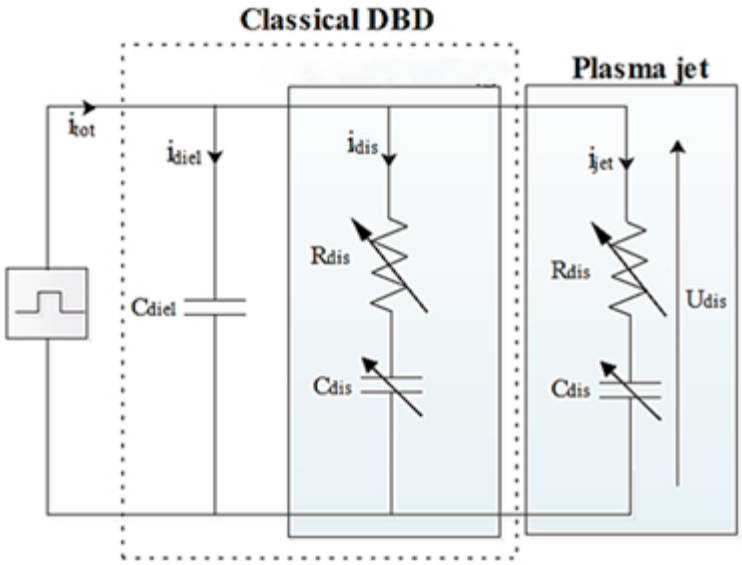

Figure 3. Electrical circuit equivalent to the plasma jet.

From the electrical circuit (Figure 3), we can deduce the appropriate mathematical equations of the discharge. Using Kirchhoff's first law, the total current is written in the following form (Equation (5)):

$$i_{tot} = i_{diel} + i_{dis} + i_{jet} \tag{5}$$

i_{diel}: dielectric current (Equation (6)), with C_{diel} being the known dielectric capacitance.

$$i_{diel} = C_{diel}\frac{dU_{dis}}{dt} \tag{6}$$

i_{dis}: streamer discharge current (Equation (7)). From Figure 2 and Kirchhoff's second law, the discharge current can be deduced as follows:

$$i_{dis} = \frac{-q_{dis}}{C_{dis}R_{dis}} + \frac{U_{dis}}{R_{dis}} \tag{7}$$

The plasma jet current, i_{jet}, is given by the following expression:

$$i_{jet} = \frac{-q_{jet}}{R_{dis}C_{dis}} + \frac{U_{dis}}{R_{dis}} \tag{8}$$

By substituting Equation (5) with Equations (6)–(8), we obtain

$$i_{tot} = C_{diel}\frac{dU_{dis}}{dt} + \frac{-q_{dis}}{R_{dis}C_{dis}} + \frac{U_{dis}}{R_{dis}} + \frac{-q_{jet}}{R_{dis}C_{dis}} + \frac{U_{dis}}{R_{dis}} \tag{9}$$

By simplifying Equation (9), we obtain

$$i_{tot} = C_{diel}\frac{dU_{dis}}{dt} - \frac{(q_{dis} + q_{jet})}{R_{dis}C_{dis}} + \frac{2U_{dis}}{R_{dis}} \tag{10}$$

Further simplifying Equation (10), we obtain

$$i_{tot} = C_{diel}\frac{dU_{dis}}{dt} - \frac{\left(\int_0^T i_{dis}dt + \int_0^T i_{jet}dt\right)}{R_{dis}C_{dis}} + \frac{2U_{dis}}{R_{dis}} \tag{11}$$

By simplifying Equation (11), we obtain

$$i_{tot} = C_{diel}\frac{dU_{dis}}{dt} - \frac{\int_0^T (i_{dis} + i_{jet})dt}{R_{dis}C_{dis}} + \frac{2U_{dis}}{R_{dis}} \tag{12}$$

By replacing the sum of the two currents $i_{dis} + i_{jet}$ according to the circuit in Figure 3, we obtain Equation (13):

$$i_{tot} = C_{diel}\frac{dU_{dis}}{dt} - \frac{\int_0^T (i_{tot} - i_{diel})dt}{R_{dis}C_{dis}} + \frac{2U_{dis}}{R_{dis}} \tag{13}$$

The next step will be devoted to the determination of the capacitance $C_{dis}(t)$ and the resistance $R_{dis}(t)$ from the mathematical equation of the electrical model (Equation (13)), using the experimental data (current (i_{diel}) and voltage (U_{dis})) and the identification method based on the recursive least squares method.

4. Recursive Least Squares Method

The recursive least squares (RLS) method is an effective approach for estimating the optimal parameters $R_{dis}(t)$ and $C_{dis}(t)$ of a model based on experimental data. Unlike simple least squares minimization, which processes the entire dataset simultaneously to provide a static estimate, the RLS method allows for real-time dynamic adaptation. At

each iteration, it updates the parameter estimates by incorporating new measurements, gradually reducing the sum of the squared differences between the experimental output and the model's predicted output [40–43]. This iterative approach is particularly beneficial in systems where conditions can change rapidly, as it ensures that the model remains relevant in the face of such fluctuations. Additionally, the RLS method requires less memory, as it retains only the essential information needed for parameter updates, without the need to store all past data. In the context of this study, the application of the RLS method improves the accuracy of the proposed circuit model while adapting to variations observed in the experimental outputs. The mathematical equation (Equation (13)) to be solved for this method is presented in matrix form (Equation (14)), facilitating iterative calculations.

$$i_{tot} - C_{diel}\frac{dU_{dis}}{dt} = \begin{bmatrix} \frac{-1}{R_{dis}C_{dis}} & \frac{2}{R_{dis}} \end{bmatrix} \begin{bmatrix} \int_0^T (i_{tot} - i_{diel})dt \\ U_{dis} \end{bmatrix} \tag{14}$$

We define the following expressions:

$$Y = i_{tot} - C_{diel}\frac{dU_{dis}}{dt} \tag{15}$$

$$\theta_N = \begin{bmatrix} \frac{-1}{R_{dis}C_{dis}} & \frac{2}{R_{dis}} \end{bmatrix} \tag{16}$$

$$\phi_N = \begin{bmatrix} \int_0^T (i_{tot} - i_{diel})dt & U_{dis} \end{bmatrix} \tag{17}$$

where i_{diel} is calculated according to Equation (6). Then,

$$Y = \theta_N {\phi_N}^T \tag{18}$$

θ_N: parameter vector to be estimated;
ϕ_N: measurement vector.

The implementation of the recursive least squares (RLS) method is described as follows. Gain K_N is calculated using Equation (19):

$$K_N = P_{N-1}\phi_N \left(\lambda + \phi^T P_{N-1}\phi_N\right)^{-1} \tag{19}$$

where P_{N-1} is the previous adaptation gain, ϕ_N is the measurement vector, and λ is the forgetting factor. Next, the prediction error ε, which represents the difference between the actual measured output i_d and the predicted output, is computed using Equation (20):

$$\varepsilon = (i_d - \phi_N \theta_{N-1}) \tag{20}$$

The parameter vector θ_N, which is to be estimated, is then updated using Equation (21):

$$\theta_N = \theta_{N-1} + P_{N-1}\phi_N \varepsilon \tag{21}$$

Finally, adaptation gain P_N is updated according to Equation (22):

$$P_N = \frac{1}{\lambda}\left(P_{N-1} - K_N \phi^T P_{N-1}\right) \tag{22}$$

Programming the recursive least squares algorithm calculates the parameter vector θ_N, using the measured data vectors (Y and ϕ_N), as well as initializations of the matrices P, θ_N, and λ. Figure 4a presents the current (i_{tot}) and voltage (U_{dis}) measurements during the discharge. The current peak observed on the left comes from a strong increase in voltage, and the one on the right indicates a strong drop in voltage. The peak that interests us is the middle one, because it represents the discharge current (total current), in this case the voltage regime takes a continuous regime. We observe that the discharge current increases

during the propagation of the ionization wave from the high voltage electrode to the ground electrode in 60 ns. This is explained by the electron avalanche which produces a charge quantity at the high voltage electrode. Also, another charge quantity occurs inside the tube during the propagation of the electrons/ions dipole from the high voltage electrode to the ground electrode when the electric field created by the space charges is superior to the one applied. Consequently, the discharge current increases. When the ionization wave links the two electrodes, it disappears, due to the discharge relaxation. This phase is characterized by the atomic de-excitation, the attachment phenomenon, and the evacuation of the charges created in the first phase. Therefore, the current decreases, as seen in Figure 4b.

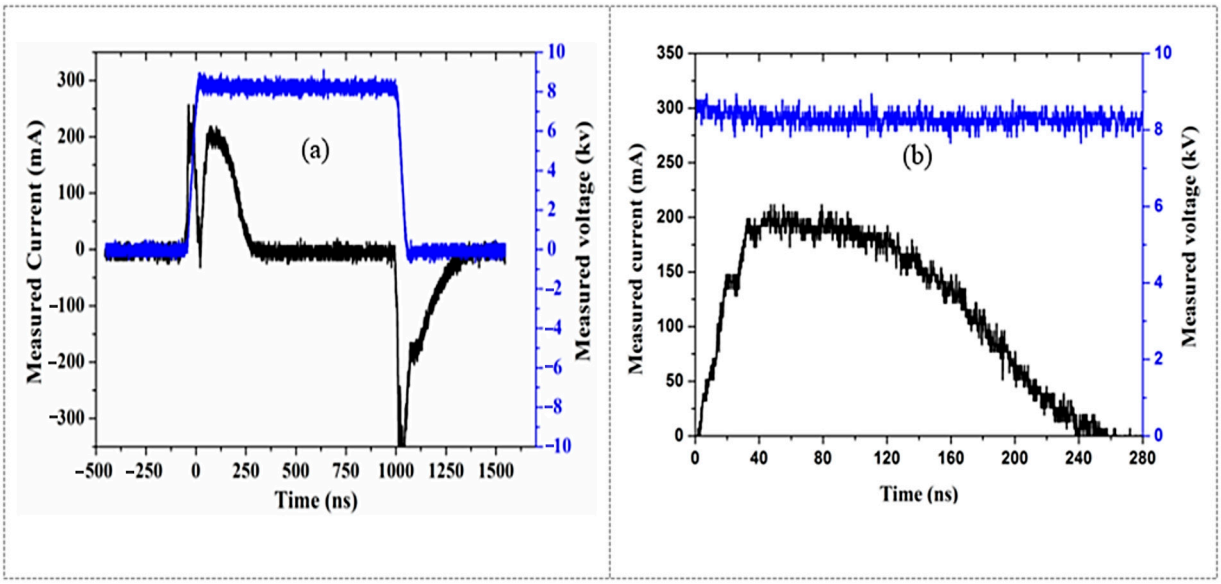

Figure 4. (**a**) Variation in voltage and discharge current with helium flow of 3 L/min, applied voltage of 8 kV, frequency of 1 kHz, and pulse width of 1 µs at atmospheric pressure, and (**b**) zoomed-in view of the discharge process.

In the following section, we will determine the electrical parameters of the proposed circuit based on the discharge current shown in Figure 4b, the voltage measured during the discharge, and the dielectric current.

5. Results and Discussion

5.1. Estimated Parameters

The resistance and capacitance of the electrical circuit at each discharge instant are determined from the estimated parameter vector θ_N, using Equation (16) and the known value of the dielectric capacitance. Figure 5 shows a significant form of estimated resistance. Before the discharge, the resistance has an infinite value due to the insulation of the tube interior, according to Ohm's law. The propagation of the electrical channel from the high voltage electrode by the ionization phenomenon causes an increase in the electron density in the medium, which leads to an increase in the discharge current during 50 nanoseconds (Figure 4b). This increase in discharge current imposes a rapid drop in resistance to its minimum of 0.1 mega-ohm. Then, the resistance curve increases to a value of 0.1 mega-ohm due to the decrease in the discharge current in the medium (Figure 4b), which is due to the discharge relaxation. The evolution of this estimated resistance is similar to that of the electrical circuit equivalent to the corona discharge reactor [39] due to the same mechanism of discharge creation in both reactors.

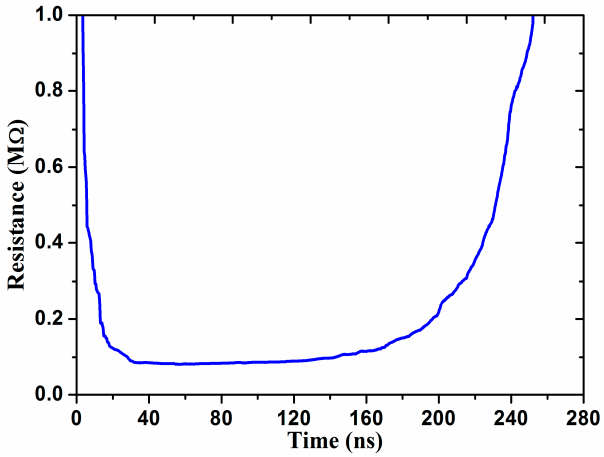

Figure 5. Estimated resistance variation with helium flow of 3 L/min, applied voltage of 8 kV, frequency of 1 kHz, and pulse width of 1 µs at atmospheric pressure.

Figure 6 shows a significant form of the estimated capacity curve. At the beginning of the discharge, the capacitance takes a low value (Equation (23)) due to the insulation of the medium (the inside of the tube). When the electric channel propagates from the high-voltage electrode, a quantity of charges accumulates in the space due to the ionization phenomenon, which imposes an increase in the capacity to its maximum according to the relation (24). Then, the capacitance curve decreases due to atomic de-excitation, the attachment phenomenon, and the progressive evacuation of charges, thus reducing the amount of charges and the estimated capacitance (Figure 6).

$$C_0 = \frac{\int i_0 dt}{u_0} \tag{23}$$

C_0: pre-discharge capacity;
i_0: pre-discharge current;
u_0: pre-discharge voltage.

$$C(t) = \frac{q_{tot}(t)}{U_{dis}} \tag{24}$$

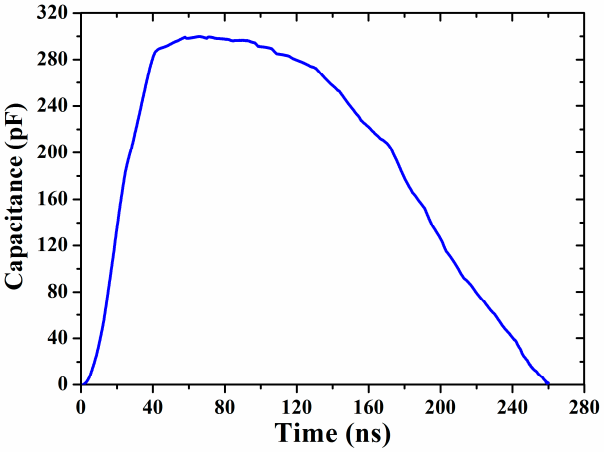

Figure 6. Estimated capacitance variation with helium flow of 3 L/min, applied voltage of 8 kV, frequency of 1 kHz, and pulse width of 1 µs at atmospheric pressure.

Thus, the final estimated capacitance and resistance curves of the proposed electrical model accurately explain the behavior of the plasma jet. These results closely resemble the electrical parameters corresponding to corona discharge [39,44], highlighting a similar

mechanism of non-thermal plasma generation in both reactors. This similarity supports the choice of the electrical model parameters for the plasma jet. The good alignment between the measured and calculated currents, as shown in Figure 7, affirms the reliability of the parameter estimation method, while the distinct patterns in the resistance and capacitance curves support the relevance of the proposed model. As a result, the resistance and capacitance of the proposed model can be effectively used in future studies to further analyze the electrical discharge of the plasma jet.

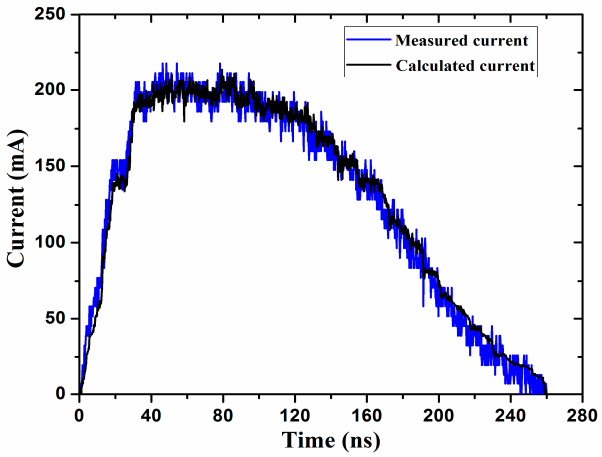

Figure 7. Comparison between measured and calculated current by estimated parameters with helium flow of 3 L/min, applied voltage of 8 kV, frequency of 1 kHz, and pulse width of 1 µs at atmospheric pressure.

5.2. Electrical Study of the Plasma Jet Reactor

The determination of the plasma jet energy efficiency by direct calculations is complicated, due to several phenomena that happen during the discharge. The proposed electrical circuit, equivalent to the plasma jet discharge, was carried out to perform an electrical study of the discharge. The estimated parameters of the proposed model will be used to calculate the discharge power and the power delivered to the reactor. The latter powers will be used to determine the energy efficiency.

5.2.1. Delivered Power

The power injected into the plasma jet reactor is calculated by multiplying the voltage U_{dis} and the circuit current i_{cal} calculated using the electrical parameters of the proposed model, as shown in relation (28).

$$P_{del} = U_{dis}\, i_{cal} \tag{25}$$

Figure 8 shows the power delivered to the plasma jet reactor. This power increase during 50 ns creates an electron avalanche by accelerating the seed electrons inside the quartz tube. In addition, this power forces the electrons/ions dipole, formed near the high voltage electrode, to propagate towards the ground electrode. The ionization wave arrives at this last electrode when the maximum power reaches 1.65 kW. Then, it decreases to relax the discharge to avoid the thermal plasma. Thus, the discharge disappears, and the electrical field regains its initial geometrical shape. At this point, the formation and propagation of new discharges become feasible. The evolution of the power delivered to the plasma jet reactor is similar to that of the corona discharge, except that the maximum power delivered to the latter reactor reaches only 0.4 kW [44]. This difference is due to the nature, volume, and dynamic of the gas, as well as the type of configuration and characteristics of the pulsed power supply.

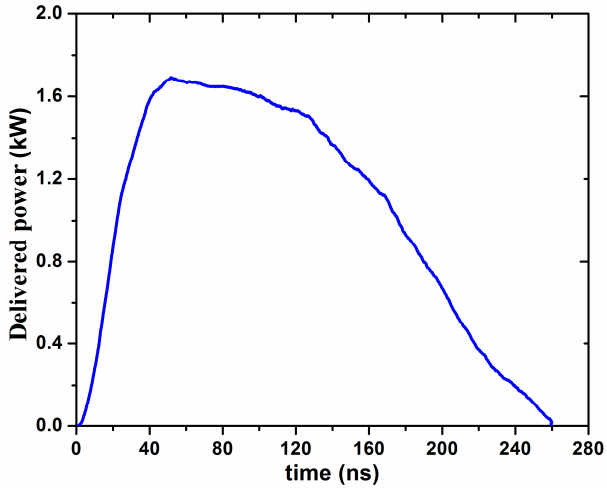

Figure 8. Variation in delivered power with helium flow of 3 L/min, applied voltage of 8 kV, frequency of 1 kHz, and pulse width of 1 µs at atmospheric pressure.

5.2.2. Discharge Power

The discharge power represents the power used during the generation of the ionization phenomenon; it is difficult to determine it by a direct method. In the electrical circuit above (Figure 3), the power lost due to the Joule effect represents the power used during the discharge, which makes it possible to determine the discharge power by using the resistance of the proposed electrical model, as shown in Equation (26).

$$P_{dis} = R_{dis}\ {I_{R_{dis}}}^2 \tag{26}$$

P_{dis}: discharge power;
$I_{R_{dis}}$: resistive current;
R_{dis}: estimated resistance.

Figure 9 shows the evolution of the discharge power. It increases to a value of 1.65 kW at the same time as the propagation of the discharge towards the ground electrode. It can be seen that the creation of the plasma jet by the ionization phenomenon in the ambient air uses a power up to 1.65 kW; then, it starts to decrease when the discharge reaches the second electrode due to the decrease in the ionization phenomenon. This period of the discharge corresponds to the atomic de-excitation, the attachment phenomenon, and the gradual evacuation of the charges. The evolution of the discharge power is similar to that of corona discharge [44].

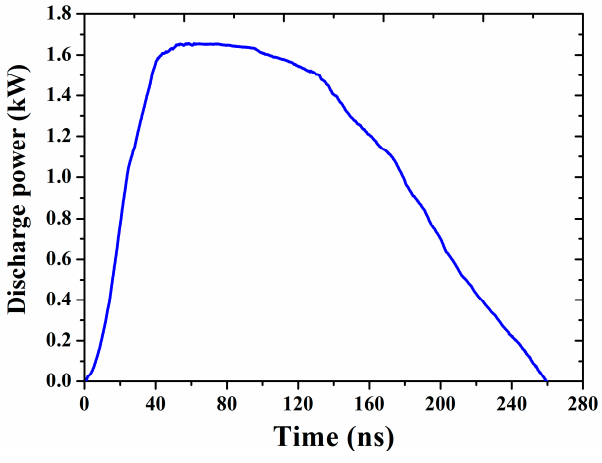

Figure 9. Variation in discharge power with helium flow of 3 L/min, applied voltage of 8 kV, frequency of 1 kHz, and pulse width of 1 µs at atmospheric pressure.

5.2.3. Plasma Energy Efficiency

Plasma energy efficiency is calculated by the ratio between the discharge power and the power delivered to the plasma jet reactor (Equation (27)). The energy efficiency increases during 50 ns due to the propagation of the discharge to the ground electrode by the ionization phenomenon. When the channels reach the second electrode, the efficiency becomes maximum at nearly 90%, and then it decreases due to the discharge relaxation phenomenon (Figure 10).

$$E_{ff} = \frac{P_u}{P_d} \tag{27}$$

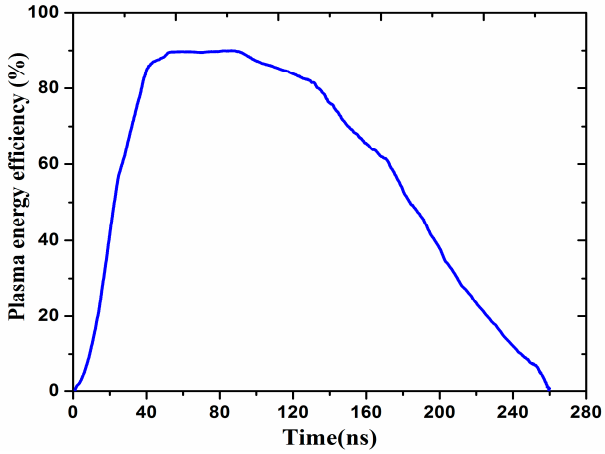

Figure 10. Variation in plasma energy efficiency with helium flow of 3 L/min, applied voltage of 8 kV, frequency of 1 kHz, and pulse width of 1 µs at atmospheric pressure.

5.3. Effect of the Applied Voltage

This part is devoted to the effect of the applied voltage (from 6 kV to 8 kV) on the electrical parameters of the proposed model, the discharge power, and the plasma jet energy efficiency.

The applied voltage increase induces a multiplication of the number of electrons created by the electron avalanche and the ionization and photoionization phenomena during the discharge propagation towards the ground electrode due to the increase in the electrical field in the medium. The discharge current inside the quartz tube is thus increased, as shown in Figure 11a. After reaching the maximum value of the current for a given applied voltage, it decreases in the second phase of the curve, due to the relaxation of the discharge. The large amount of charge created in the first phase prolongs the duration of the atomic de-excitation, the attachment phenomenon, and the progressive evacuation of charges at high applied voltage. Thus, the discharge current slowly decreases from 6 kV to 8 kV during the passage.

Figure 11b shows the resistance evolution estimated for different applied voltages. It is seen that the resistance reaches a very fast minimum value due to the rapid increase in the discharge current at its maximum (Figure 11a) when passing from a voltage of 6 kV to 8 kV (according to Ohm's law). In addition, its minimum value decreases due to the increase in the maximum current. In the relaxation phase, the resistance returns very quickly to its initial state when the voltage is increased due to a slow decrease in the discharge current as explained above (according to Ohm's law). At high applied voltages, a large amount of charge is generated inside the quartz tube due to a strong ionization phenomenon, resulting in a large capacitance (Figure 11c).

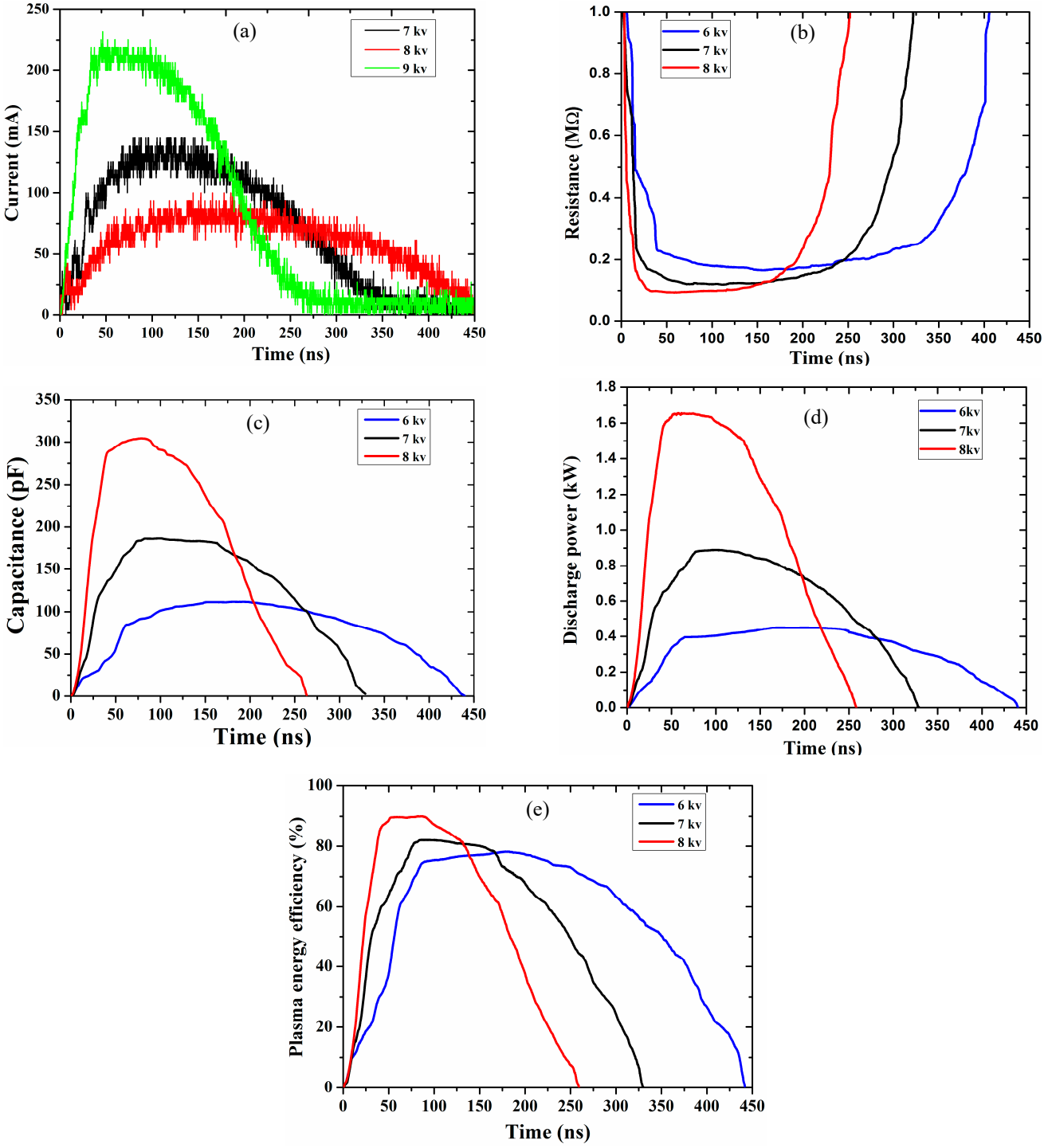

Figure 11. Effect of applied voltage on discharge current (**a**), resistance (**b**), capacitance (**c**), discharge power (**d**), and plasma energy efficiency (**e**) with helium flow rate of 3 L/min, frequency of 1 kHz, and pulse width of 1 µs at atmospheric pressure.

The discharge power increases from 0.4 kW to 1.6 kW as the applied voltage increases (Figure 11d). This is due to a strong ionization phenomenon for high applied voltage as explained above, which consumes more power to generate non-thermal plasma. Increasing the power improves the plasma energy efficiency form 75% up to 90% (Figure 11e).

6. Conclusions

This study presents an electrical model of a plasma jet reactor, aiming to improve energy efficiency through precise parameter estimation. Using the recursive least squares (RLS) method, we developed an equivalent electrical circuit to characterize the plasma discharge. The close alignment between the experimentally measured current and the calculated current, as well as the distinct evolution of the estimated electrical parameters, underscores the effectiveness of our parameter estimation method. By applying this model, we were able to determine the energy delivered to the reactor and the energy consumed during discharge, leading to an understanding of plasma jet energy efficiency.

Our findings reveal that the energy efficiency of the plasma jet can be significantly improved by increasing the applied voltage, with efficiency values rising from 75% to 90% when the voltage is increased from 6 kV to 8 kV. This model thus enables control over the reactor's energy performance, providing a basis for optimizing operating conditions to achieve maximum efficiency.

In future work, priority will be given to validating this model with independent data, aiming to further reinforce its applicability. This step will fully assess the model's predictive capabilities beyond the current experimental setup, facilitating continued advancements in energy-efficient plasma technologies.

Author Contributions: Conceptualization, A.H. and K.S.; methodology, A.H. and K.S.; software, K.S.; validation, A.A. and N.M.; formal analysis, A.H. and K.S.; investigation, A.A. and N.M.; writing—original draft preparation, A.H. and K.S.; writing—review and editing, A.H., K.S., A.A. and N.M.; visualization, A.H. and K.S.; supervision, A.A. and N.M.; project administration, A.A. and N.M. All authors have read and agreed to the published version of the manuscript.

Funding: This research received no external funding.

Institutional Review Board Statement: Not applicable.

Informed Consent Statement: Not applicable.

Data Availability Statement: The data presented in this study are available on request from the corresponding author.

Conflicts of Interest: The authors declare no conflict of interest.

References

1. Koga-Ito, C.Y.; Kostov, K.G.; Miranda, F.S.; Milhan, N.V.M.; Azevedo Neto, N.F.; Nascimento, F.; Pessoa, R.S. Cold Atmospheric Plasma as a Therapeutic Tool in Medicine and Dentistry. *Plasma Chem. Plasma Process.* **2024**, *44*, 1393–1429. [CrossRef]
2. Adesina, K.; Lin, T.-C.; Huang, Y.-W.; Locmelis, M.; Han, D. A Review of Dielectric Barrier Discharge Cold Atmospheric Plasma for Surface Sterilization and Decontamination. *IEEE Trans. Radiat. Plasma Med. Sci.* **2024**, *8*, 295–306. [CrossRef]
3. Walden, R.; Goswami, A.; Scally, L.; McGranaghan, G.; Cullen, P.J.; Pillai, S.C. Nonthermal plasma technologies for advanced functional material processing and current applications: Opportunities and challenges. *J. Environ. Chem. Eng.* **2024**, *12*, 113541. [CrossRef]
4. Das, S.; Mishra, B.; Mohapatra, S.; Tripathi, B.P.; Kar, S.; Bhatt, S. Efficacy of argon cold atmospheric pressure plasma jet on hospital surface decontamination and its impact on the surface property. *Phys. Scr.* **2024**, *99*, 025601. [CrossRef]
5. Gowri, K.N.; Güler, H.K.; King, M.W. Plasma in biomedical applications. In *Advances in Plasma Treatment of Textile Surfaces*; Woodhead Publishing: Sawston, UK, 2024. Available online: https://www.sciencedirect.com/science/article/pii/B9780443190797000099 (accessed on 30 September 2024).
6. Wree, J.L.; Rogalla, D.; Ostendorf, A.; Schierbaum, K.D.; Devi, A. Plasma-Enhanced Atomic Layer Deposition of Molybdenum Oxide Thin Films at Low Temperatures for Hydrogen Gas Sensing. *ACS Appl. Mater. Interfaces* **2022**, *15*, 14502–14512. [CrossRef]
7. Laghi, G.; Franco, D.; Condorelli, G.G.; Gallerani, R.; Guglielmino, S.; Laurita, R.; Morganti, D.; Traina, F.; Conoci, S.; Gherardi, M. Control strategies for atmospheric pressure plasma polymerization of fluorinated silane thin films with antiadhesive properties. *Plasma Process. Polym.* **2023**, *20*, 2200194. [CrossRef]
8. Farhadi, K.; Romanos, G.E. Plasma Cleaning for Implant Surfaces to Improve Implant Success. In *Saving Dental Implants*; Wiley: Hoboken, NJ, USA, 2024; pp. 534–544. [CrossRef]
9. Suschek, C. *Plasma Applications in Biomedicine*; MDPI: Basel, Switzerland, 2024. Available online: https://www.mdpi.com/books/reprint/9534 (accessed on 30 September 2024).

10. Kazemi, A.; Nicol, M.J.; Bilén, S.G.; Kirimanjeswara, G.S.; Knecht, S.D. Cold Atmospheric Plasma Medicine: Applications, Challenges, and Opportunities for Predictive Control. *Plasma* **2024**, *7*, 233–257. [CrossRef]
11. Li, Y.; Tan, S.; Liu, D.; Zhang, Y. Molecular dynamics simulation research on the interaction between plasma and living organisms: A comprehensive review. *Plasma Process. Polym.* **2024**, *21*, 2300119. [CrossRef]
12. Dufour, T. From basics to frontiers: A comprehensive review of plasma-modified and plasma-synthesized polymer films. *Polymers* **2023**, *15*, 3607. [CrossRef]
13. Rahman, T.U.; Roy, H.; Fariha, A.; Shoronika, A.Z.; Al-Mamun, M.R.; Islam, S.Z.; Islam, M.S.; Marwani, H.M.; Islam, A.; Alsukaibi, A.K.; et al. Progress in plasma doping semiconductor photocatalysts for efficient pollutant remediation and hydrogen generation. *Sep. Purif. Technol.* **2023**, *320*, 124141. [CrossRef]
14. Koinuma, H.; Ohkubo, H.; Hashimoto, T.; Inomata, K.; Shiraishi, T.; Miyanaga, A.; Hayashi, S. Development and application of a microbeam plasma generator. *Appl. Phys. Lett.* **1992**, *60*, 816. [CrossRef]
15. Stoffels, E.; Flikweert, A.J.; Stoffels, W.W.; Kroesen, G. Plasma needle: A non-destructive atmospheric plasma source for fine surface treatment of (bio)materials. *Plasma Sources Sci. Technol.* **2002**, *11*, 383. [CrossRef]
16. Laroussi, M.; Lu, X. Room-temperature atmospheric pressure plasma plume for biomedical applications. *Appl. Phys. Lett.* **2005**, *87*, 113902. [CrossRef]
17. Förster, S.; Mohr, C.; Viöl, W. Investigations of an atmospheric pressure plasma jet by optical emission spectroscopy. *Surf. Coat. Technol.* **2005**, *200*, 827. [CrossRef]
18. Teschke, M.; Kedzierski, J.; Finantu-Dinu, E.G.; Korzec, D.; Engemann, J. High speed photographs of a dielectric barrier atmospheric pressure plasma jet. *IEEE Trans. Plasma Sci.* **2005**, *33*, 310. [CrossRef]
19. Zhang, J.; Sun, J.; Wang, D.; Wang, X. A novel cold plasma jet generated by atmospheric dielectric barrier capillary discharge. *Thin Solid Film.* **2006**, *506*, 404. [CrossRef]
20. Walsh, J.L.; Shi, J.J.; Kong, M.G. Contrasting characteristics of pulsed and sinusoidal cold atmospheric plasma jets. *Appl. Phys. Lett.* **2006**, *88*, 171501. [CrossRef]
21. Cheng, C.; Peng, L.; Lei, X.; Li-Ye, Z.; Ru-Juan, Z.; Wen-Rui, Z. Development of a new atmospheric pressure cold plasma jet generator and application in sterilization. *Chin. Phys.* **2006**, *15*, 1544. [CrossRef]
22. Kim, D.B.; Rhee, J.K.; Moon, S.Y.; Choe, W. Study of geometrical and operational parameters controlling the low frequency microjet atmospheric pressure plasma characteristics. *Appl. Phys. Lett.* **2006**, *89*, 061502. [CrossRef]
23. Hong, Y.C.; Uhm, H.S.; Cheol, Y. Microplasma jet at atmospheric pressure. *Appl. Phys. Lett.* **2006**, *89*, 221504. [CrossRef]
24. Lu, X.P.; Laroussi, M. Dynamics of an atmospheric pressure plasma plume generated by submicrosecond voltage pulses. *J. Appl. Phys.* **2006**, *100*, 063302. [CrossRef]
25. Sands, B.L.; Ganguly, B.N.; Tachibana, K. A streamer-like atmospheric pressure plasma jet. *Appl. Phys. Lett.* **2008**, *92*, 151503. [CrossRef]
26. Naidis, G.V. Modelling of streamer propagation in atmospheric-pressure helium plasma jets. *J. Phys. D Appl. Phys.* **2010**, *43*, 402001. [CrossRef]
27. Jánský, J.; Bourdon, A. Simulation of helium discharge ignition and dynamics in thin tubes at atmospheric pressure. *Appl. Phys. Lett.* **2011**, *99*, 161504. [CrossRef]
28. Breden, D.; Miki, K.; Raja, L.L. Computational study of cold atmospheric nanosecond pulsed helium plasma jet in air. *Appl. Phys. Lett.* **2011**, *99*, 111501. [CrossRef]
29. Yousfi, M.; Eichwald, O.; Merbahi, N.; Jomaa, N. Analysis of ionization wave dynamics in low-temperature plasma jets from fluid modeling supported by experimental investigations. *Plasma Sources Sci. Technol.* **2012**, *21*, 045003. [CrossRef]
30. Boeuf, J.P.; Yang, L.L.; Pitchford, L.C. Dynamics of a guided streamer ('plasma bullet') in a helium jet in air at atmospheric pressure. *J. Phys. D Appl. Phys.* **2012**, *46*, 015201. [CrossRef]
31. Khacef, A.; Cormier, J.M. Pulsed sub-microsecond dielectric barrier discharge treatment of simulated glass manufacturing industry flue gas: Removal of SO_2 and NO_x. *J. Phys. D Appl. Phys.* **2006**, *39*, 1078–1083. [CrossRef]
32. Motret, O.; Hibert, C.; Pellerin, S.; Pouvesle, J.M. Rotational temperature measurements in atmospheric pulsed dielectric barrier discharge—Gas temperature and molecular fraction effects. *J. Phys. D Appl. Phys.* **2000**, *33*, 1493–1498. [CrossRef]
33. Odic, E.; Dhainaut, M.; Petit, M.; Goldman, A.; Goldman, M.; Karimi, C. Approach of the Physical and Chemical Specic Properties of Pulsed Surface Dielectric Barrier Discharges in Air at Atmospheric Pressure. *J. Adv. Oxid. Technol.* **2003**, *6*, 41–47.
34. Pipa, A.; Brandenburg, R. The Equivalent Circuit Approach for the Electrical Diagnostics of Dielectric Barrier Discharges: The Classical Theory and Recent Developments. *Atoms* **2019**, *7*, 14. [CrossRef]
35. Rueda, V.; Wiesner, A.; Diez, R.; Piquet, H. Power Estimation of a Current Supplied DBD Considering the Transformer Parasitic Elements. *IEEE Trans. Ind. Appl.* **2019**, *55*, 6567–6575. [CrossRef]
36. Florez, D.; Schitz, D.; Piquet, H.; Diez, R. Efficiency of an Exciplex DBD Lamp Excited Under Different Methods. *IEEE Trans. Plasma Sci.* **2018**, *46*, 140–147. [CrossRef]
37. Rueda, V.; Diez, R.; Bente, N.; Piquet, H. Combined Image Processing and Equivalent Circuit Approach for the Diagnostic of Atmospheric Pressure DBD. *Appl. Sci.* **2022**, *12*, 8009. [CrossRef]
38. Fang, Z.; Shao, T.; Yang, J.; Zhang, C. Discharge processes and an electrical model of atmospheric pressure plasma jets in argon. *Eur. Phys. J. D* **2016**, *70*, 3. [CrossRef]

39. Saber, K.; Guedah, H.; Abahazem, A.; Merbahi, N.; Yousfi, M. Electrical equivalent circuit and modeling of a pulsed air corona discharge. *Mater. Today Proc.* **2020**, *24*, 119–124. [CrossRef]
40. Landau, I.-D. *Identification des Systems*; HERME Editions collection pédagogique d'automatique; HERMES: New Castle, PA, USA, 1998; ISBN 2-86601-683-1.
41. Díez, R.; Salanne, J.-P.; Piquet, H.; Bhosle, S.; Zissis, G. Predictive model of a DBD lamp for power supply design and method for the automatic identification of its parameters. *Eur. Phys. J. Appl. Phys.* **2007**, *37*, 307–313. [CrossRef]
42. Grillenzoni, C. Optimal recursive estimation of dynamic models. *J. Am. Stat. Assoc.* **1994**, *89*, 777–787. [CrossRef]
43. Barlaud, M.; Alengrin, G.; Menez, J.; Grenier, Y.; Aboutajdine, D. Méthodes d'identification paramétrique pour des signaux non-stationnaires perturbés par un bruit blanc. In Proceedings of the 11th Colloque on Signal and Image Processing, Gretsi, Nice, France, 1–5 June 1987; pp. 749–752.
44. Saber, K.; Abahazem, A.; Merbahi, N.; Yousfi, M. Plasma energy efficiency in tip-to-plane air corona discharges at atmospheric pressure. *J. Electrost.* **2022**, *115*, 103642. [CrossRef]